


# Low-energy effective theory and symmetry classification of flux phases on the kagome lattice

Xilin Feng <sup>1,2</sup> Yi Zhang <sup>3</sup> Kun Jiang<sup>1,\*</sup> and Jiangping Hu<sup>1,3,†</sup>

<sup>1</sup>Beijing National Laboratory for Condensed Matter Physics and Institute of Physics, Chinese Academy of Sciences, Beijing 100190, China

<sup>2</sup>School of Physical Sciences, University of Chinese Academy of Sciences, Beijing 100190, China

<sup>3</sup>Kavli Institute of Theoretical Sciences, University of Chinese Academy of Sciences, Beijing 100190, China

 (Received 19 June 2021; revised 13 October 2021; accepted 13 October 2021; published 22 October 2021)

Motivated by recent experiments on  $AV_3Sb_5$  ( $A = K, Rb, Cs$ ), the chiral flux phase has been proposed to explain time-reversal symmetry breaking. To fully understand the physics behind the chiral flux phase, we construct a low-energy effective theory based on the van Hove points around the Fermi surface. The possible symmetry-breaking states and their classifications of the low-energy effective theory are completely studied, especially the flux phases on the kagome lattice. In addition, we discuss the relations between the low-energy symmetry breaking orders, the chiral flux, and charge bond orders. We find all possible 183 flux phases on the kagome lattice within a  $2 \times 2$  unit cell by brute-force approach and classify them by point-group symmetry. Among the 183 phases, we find 3 classes in a  $1 \times 1$  unit cell, 8 classes in a  $1 \times 2$  unit cell, and 18 classes in a  $2 \times 2$  unit cell, respectively. These results provide a full picture of the time-reversal symmetry breaking in kagome lattices.

DOI: [10.1103/PhysRevB.104.165136](https://doi.org/10.1103/PhysRevB.104.165136)

## I. INTRODUCTION

In condensed matter physics, there are many interesting unconventional flux phases. For instance, the Haldane model on the honeycomb lattice is the most well-known flux phase, where opposite flux loops are formed in different sublattice triangles respectively [1]. Meanwhile, flux phases are also widely discussed in high-temperature cuprate superconductors after the seminal work by Affleck and Marston in  $t$ - $J$  models [2–4]. Generalizing this discussion, Varma proposed a loop-current phase formed in the Cu-O triangles [5] and Chakravarty *et al.* proposed the  $d$ -density wave state with staggered flux in Cu square plaquettes [6]. Both states break the time-reversal symmetry and are supposed to be the candidates for the pseudogap in cuprates [5,7–9]. In addition, flux phases in square lattices, hexagonal lattices, and other systems have been widely discussed [10–17]. Although there are plenty of theoretical proposals, whether flux phases can be found in condensed matter is still an open question.

Recently, the unconventional charge density wave (CDW) order has been found in nonmagnetic  $AV_3Sb_5$  ( $A = K, Rb, Cs$ ) [18,19] by scanning tunneling microscopy (STM) [20] and anomalous Hall effect [21,22]. This CDW breaks the time-reversal symmetry and is further supported by recent muon spin spectroscopy measurements [20,23]. To explain this time-reversal symmetry breaking phenomena, many interesting theoretical proposals have been discussed in the kagome lattice [24–27], especially the chiral flux phase (CFP) [24], which carry unique nontrivial topological properties. How-

ever, this previous CFP proposal [24] only includes one particular flux pattern. Several important questions were left behind, including why the flux pattern is selected, how many flux phases are in the kagome lattice, and how these flux phases are classified by symmetry.

In this paper we construct a low-energy effective theory using the dominant scattering between van Hove (vH) points around Fermi surfaces (FSs) to study the CFPs. We classify the possible symmetry breaking states by point-group operations, including on-site charge orders, bond orders, and flux phases. The relations between low-energy breaking orders to the physical orders in real space are completely established, especially the chiral flux phase, charge bond orders proposed in previous works [24]. We calculate all kinds of flux configuration in real space within a  $2 \times 2$  unit cell and classify them by symmetry. Our result establishes a full physical picture of the CFPs in  $AV_3Sb_5$  ( $A = K, Rb, Cs$ ).

Before any detailed discussion, we first go through the symmetry group of the kagome lattice, which will be frequently used in the following discussions. The point group of the kagome lattice and  $AV_3Sb_5$  is  $D_{6h}$ . The  $D_{6h}$  contains three generators: the  $C_6$  rotation along the  $z$  axis, the inversion operation  $I$  at the kagome hexagonal center, and the mirror symmetry  $\sigma_v$  about the  $yz$  plane, as illustrated in Fig. 1(a). Multiplying  $C_6$  rotation generates the  $C_3$  and  $C_2$  rotations. Multiplying  $C_6$ ,  $C_3$ , and  $C_2$  rotations with  $I$  generates  $S_6$ ,  $S_3$ , and  $\sigma_h$ . Multiplying  $C_6$ ,  $C_3$ , and  $C_2$  rotations with  $\sigma_v$  generate other  $\sigma_v$  and  $\sigma_d$ . Multiplying  $\sigma_v$  with  $I$  generates other  $C_2'$ s and  $C_2''$ s. In addition, each unit cell of the kagome lattice contains three sublattices, labeled as  $A$ ,  $B$ ,  $C$ , as shown in Fig. 1(a). The unit cell forms a triangular lattice with translation vector  $\mathbf{a}_1 = (1, 0)$  and  $\mathbf{a}_2 = (\frac{1}{2}, \frac{\sqrt{3}}{2})$ . This translation group is labeled as  $T(\mathbf{a}_1, \mathbf{a}_2)$ .

\*jiangkun@iphy.ac.cn

†jphu@iphy.ac.cn

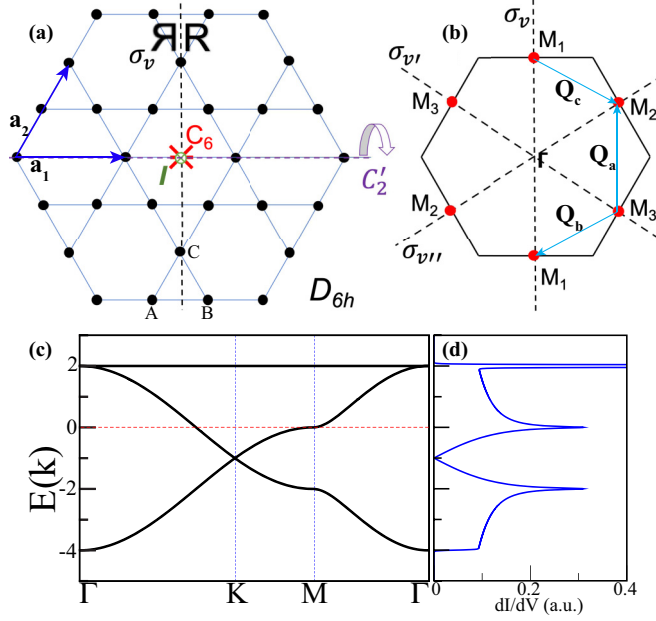


FIG. 1. (a) Kagome lattice point-group  $D_{6h}$  and its operations:  $C_6$  rotation (red), inversion  $I$  operation (green), mirror symmetry  $\sigma_v$  about the  $yz$  plane (black), and  $C_2'$  rotation along the  $x$  axis (purple). The translation vectors are  $\mathbf{a}_1$  and  $\mathbf{a}_2$ . And the sublattice index is labeled as  $A, B, C$  in each unit cell. (b) Brillouin zone of the kagome lattice and three dominated van Hove points  $M_1 = (0, \frac{\pi}{\sqrt{3}})$ ,  $M_2 = (\frac{\pi}{2}, \frac{\pi}{2\sqrt{3}})$ , and  $M_3 = (\frac{\pi}{2}, -\frac{\pi}{2\sqrt{3}})$ . The corresponding scatter vectors are also labeled as  $\mathbf{Q}_a = \{0, \frac{2\pi}{\sqrt{3}}\}$ ,  $\mathbf{Q}_b = \{-\pi, -\frac{\pi}{\sqrt{3}}\}$ , and  $\mathbf{Q}_c = \{\pi, -\frac{\pi}{\sqrt{3}}\}$ . (c) Band structure for the kagome lattice. (d) Tunneling density of states (DoS) of the tight-binding model for (c), which can be measured by the differential conductance ( $dI/dV$ ).

## II. THE LOW-ENERGY EFFECTIVE THEORY AND $3Q$ SCATTERING BETWEEN VH POINTS

As discussed in our previous work [24,28,29], the electronic properties, especially the CDW orders, of  $AV_3Sb_5$  materials are dominated by the  $Vd$  orbitals, which can be captured by a minimum single orbital model [24,28,29]. To capture the essential physics behind the  $AV_3Sb_5$  charge density wave, a nearest neighbor tight-binding model on the kagome lattice can be applied without losing generality. In the basis of  $c_k = (c_{k,A}, c_{k,B}, c_{k,C})$ , the Hamiltonian can be written as  $H_0 = \sum_k c_k^\dagger H_k c_k$ , where

$$H_k = \begin{bmatrix} -\mu & -2t \cos(k_1/2) & -2t \cos(k_2/2) \\ -2t \cos(k_1/2) & -\mu & -2t \cos(k_3/2) \\ -2t \cos(k_2/2) & -2t \cos(k_3/2) & -\mu \end{bmatrix} \quad (1)$$

and  $k_1 = k_x$ ,  $k_2 = \frac{1}{2}k_x + \frac{\sqrt{3}}{2}k_y$ , and  $k_3 = -\frac{1}{2}k_x + \frac{\sqrt{3}}{2}k_y$ .  $\mu$  is the chemical potential and the hopping  $t$  is chosen to be 1 as the energy unit. The band structure for the kagome model is shown in Fig. 1(c) and the electron filling is tuned to the  $5/4$  vH filling ( $5/12$  band filling), where the Fermi level crosses the van Hove  $M$  points. Throughout this paper we use the Brillouin zone (BZ) filling notation, which is equal to the band filling divided by 3. Owing to the singular density of states [as shown in Fig. 1(d)], the low-energy physics of  $AV_3Sb_5$

should be dominated by the quasiparticles around the vH points. As indicated in the Brillouin zone of the kagome lattice shown in Fig. 1(b), there is three vH points at  $M_1 = (0, \frac{\pi}{\sqrt{3}})$ ,  $M_2 = (\frac{\pi}{2}, \frac{\pi}{2\sqrt{3}})$ , and  $M_3 = (\frac{\pi}{2}, -\frac{\pi}{2\sqrt{3}})$ . The symmetry breaking states of  $AV_3Sb_5$  are widely believed to come from the scattering between  $M$  points with momentum transfer  $\mathbf{Q}_a = \{0, \frac{2\pi}{\sqrt{3}}\}$ ,  $\mathbf{Q}_b = \{-\pi, -\frac{\pi}{\sqrt{3}}\}$ , and  $\mathbf{Q}_c = \{\pi, -\frac{\pi}{\sqrt{3}}\}$ .

Hence, we can downfold the model and construct a low-energy effective model based on the quasiparticles at the three vH points as

$$\psi_M = (\psi_{M_1}, \psi_{M_2}, \psi_{M_3})^T. \quad (2)$$

Similar approaches in triangular and honeycomb lattices are discussed in Ref. [10]. And for the  $5/4$  filling kagome lattice, the eigenstate of vH has the exact sublattice index owing to symmetry. Specifically,  $\psi_{M_1}$  is exactly coming from sublattice  $C$ ,  $\psi_{M_2}$  is exactly coming from sublattice  $A$ , and  $\psi_{M_3}$  is exactly coming from sublattice  $B$ .

From a symmetry point of view, the group of wave vectors at  $M$  point is  $D_{2h}$  and  $M_1, M_2, M_3$  form the star of  $M$  related by the  $C_6$  rotation. For simplicity we choose five representative elements  $\{C_6, C_3, \sigma_v, \sigma_v', \sigma_v''\}$  of  $D_{6h}$  to classify the symmetry operations of  $\psi_M$ . The three mirror operations  $\sigma_v, \sigma_v', \sigma_v''$  along the three hexagonal axes are also indicated in Fig. 1(b). The matrix elements of each operation in  $\psi_M$  basis are

$$\begin{aligned} C_6 &= \begin{pmatrix} 0 & 1 & 0 \\ 0 & 0 & 1 \\ 1 & 0 & 0 \end{pmatrix}, & C_3 &= \begin{pmatrix} 0 & 0 & 1 \\ 1 & 0 & 0 \\ 0 & 1 & 0 \end{pmatrix}, \\ \sigma_v &= \begin{pmatrix} 0 & 0 & 1 \\ 0 & 1 & 0 \\ 1 & 0 & 0 \end{pmatrix}, & \sigma_{v'} &= \begin{pmatrix} 0 & 1 & 0 \\ 1 & 0 & 0 \\ 0 & 0 & 1 \end{pmatrix}, \\ \sigma_{v''} &= \begin{pmatrix} 1 & 0 & 0 \\ 0 & 0 & 1 \\ 0 & 1 & 0 \end{pmatrix}. \end{aligned} \quad (3)$$

In  $\psi_M$  basis, any symmetry breaking order parameters  $\hat{\Delta}_\alpha$  can be written as

$$\hat{\Delta}_\alpha = \sum_i \Delta_{\alpha,i} \hat{\Gamma}_i, \quad (4)$$

where the  $\hat{\Gamma}_i$  are the eight generators of  $SU(3)$  group in the defining representation, which are also known as the Gell-Mann matrices [10],

$$\begin{aligned} \Gamma_1 &= \begin{pmatrix} 0 & 1 & 0 \\ 1 & 0 & 0 \\ 0 & 0 & 0 \end{pmatrix}, & \Gamma_2 &= \begin{pmatrix} 0 & -i & 0 \\ i & 0 & 0 \\ 0 & 0 & 0 \end{pmatrix}, \\ \Gamma_3 &= \begin{pmatrix} 1 & 0 & 0 \\ 0 & -1 & 0 \\ 0 & 0 & 0 \end{pmatrix}, & \Gamma_4 &= \begin{pmatrix} 0 & 0 & 1 \\ 0 & 0 & 0 \\ 1 & 0 & 0 \end{pmatrix}, \\ \Gamma_5 &= \begin{pmatrix} 0 & 0 & -i \\ 0 & 0 & 0 \\ i & 0 & 0 \end{pmatrix}, & \Gamma_6 &= \begin{pmatrix} 0 & 0 & 0 \\ 0 & 0 & 1 \\ 0 & 1 & 0 \end{pmatrix}, \\ \Gamma_7 &= \begin{pmatrix} 0 & 0 & 0 \\ 0 & 0 & -i \\ 0 & i & 0 \end{pmatrix}, & \Gamma_8 &= \frac{1}{\sqrt{3}} \begin{pmatrix} 1 & 0 & 0 \\ 0 & 1 & 0 \\ 0 & 0 & -2 \end{pmatrix}. \end{aligned} \quad (5)$$

TABLE I. The symmetry relations of  $\hat{\Gamma}_i$  under the operations in  $D_{6h}$ .

|              | $\Gamma_1$ | $\Gamma_2$  | $\Gamma_4$ | $\Gamma_5$  | $\Gamma_6$ | $\Gamma_7$  | $\Gamma_3$  | $\Gamma_8$  |
|--------------|------------|-------------|------------|-------------|------------|-------------|---|---|
| $C_6$        | $\Gamma_4$ | $-\Gamma_5$ | $\Gamma_6$ | $-\Gamma_7$ | $\Gamma_1$ | $\Gamma_2$  | $-\frac{1}{2}\Gamma_3 - \frac{\sqrt{3}}{2}\Gamma_8$ | $\frac{\sqrt{3}}{2}\Gamma_3 - \frac{1}{2}\Gamma_8$  |
| $C_3$        | $\Gamma_6$ | $\Gamma_7$  | $\Gamma_1$ | $-\Gamma_2$ | $\Gamma_4$ | $\Gamma_5$  | $-\frac{1}{2}\Gamma_3 + \frac{\sqrt{3}}{2}\Gamma_8$ | $-\frac{\sqrt{3}}{2}\Gamma_3 - \frac{1}{2}\Gamma_8$ |
| $\sigma_v$   | $\Gamma_6$ | $-\Gamma_7$ | $\Gamma_4$ | $-\Gamma_5$ | $\Gamma_1$ | $-\Gamma_2$ | $\frac{1}{2}\Gamma_3 - \frac{\sqrt{3}}{2}\Gamma_8$  | $-\frac{\sqrt{3}}{2}\Gamma_3 - \frac{1}{2}\Gamma_8$ |
| $\sigma'_v$  | $\Gamma_1$ | $-\Gamma_2$ | $\Gamma_6$ | $\Gamma_7$  | $\Gamma_4$ | $\Gamma_5$  | $-\Gamma_3$   | $\Gamma_8$  |
| $\sigma''_v$ | $\Gamma_4$ | $\Gamma_5$  | $\Gamma_1$ | $\Gamma_2$  | $\Gamma_6$ | $-\Gamma_7$ | $\frac{1}{2}\Gamma_3 + \frac{\sqrt{3}}{2}\Gamma_8$  | $\frac{\sqrt{3}}{2}\Gamma_3 - \frac{1}{2}\Gamma_8$  |

The symmetry properties of  $\hat{\Gamma}_i$  under the operations in  $D_{6h}$  with  $D(R_i)\Gamma_i D(R_i)^{-1} = D_{ij}\Gamma_j$ , as summarized in Table I. From Table I we can find that the  $\hat{\Gamma}_i$  can be divided into three classes by operations in  $D_{6h}$ . They are  $\hat{\Delta}_b = \{\Gamma_1, \Gamma_4, \Gamma_6\}$ ,  $\hat{\Delta}_\phi = \{\Gamma_2, \Gamma_5, \Gamma_7\}$ ,  $\hat{\Delta}_s = \{\Gamma_3, \Gamma_8\}$ .

Hence, the order parameters can be classified based on the above transformation relations. For  $\hat{\Delta}_b$  class, the matrix element for each  $\hat{\Delta}_b$  is real and gives rise to the interscattering between  $M$  points. Since  $\psi_{Mi}$  carries the sublattice index, the  $\hat{\Delta}_b$  corresponds to the bonding between sublattices. And the order parameters can be further classified as

$$\hat{\Delta}_{b,1} = \Delta_{b,1}(\Gamma_1 + \Gamma_4 + \Gamma_6), \quad (6)$$

$$\hat{\Delta}_{b,2} = \Delta_{b,2}(\Gamma_1 - \Gamma_4), \quad (7)$$

$$\hat{\Delta}_{b,3} = \Delta_{b,3}(\Gamma_1 - \Gamma_6), \quad (8)$$

where the  $\hat{\Delta}_{b,1}$  forms the  $A_{1g}$  representation of the point-group  $D_{6h}$  with breaking the translation symmetry. The  $\hat{\Delta}_{b,2}$  and  $\hat{\Delta}_{b,3}$  forms the  $B_{1g}$  representation of two different  $D_{2h}$  groups. These two different  $D_{2h}$  groups are generated by three generators:  $C_2$  rotation along the  $z$  axis,  $\sigma''_v$  or  $\sigma_v$  for different  $D_{2h}$  groups, respectively, and inversion operator  $\mathcal{I}$ .

In the same spirit, the  $\hat{\Delta}_\phi$  class corresponds to flux phase and the order parameters can be classified as

$$\hat{\Delta}_{\phi,1} = \Delta_{\phi,1}(\Gamma_2 - \Gamma_5 + \Gamma_7), \quad (9)$$

$$\hat{\Delta}_{\phi,2} = \Delta_{\phi,2}(\Gamma_5 + \Gamma_7), \quad (10)$$

$$\hat{\Delta}_{\phi,3} = \Delta_{\phi,3}(\Gamma_2 + \Gamma_5). \quad (11)$$

The  $\hat{\Delta}_{\phi,1}$  forms the  $A_{1g}$  representation of the magnetic point-group  $D_{6h}^*$ . This magnetic point-group  $D_{6h}^*$  is normally written as  $D_{6h}^*(C_{6h})$ , where  $C_{6h}$  is the invariant subgroup of  $D_{6h}$ . The  $D_{6h}^*$  is formed by keeping elements of  $D_{6h}$  belonging to the  $C_{6h}$  and multiplying the remaining elements by time-reversal operator  $\mathcal{T}$ . Hence, the  $D_{6h}^*$  are generated by three generators:  $C_6$  rotation along the  $z$  axis, inversion operator  $\mathcal{I}$ , and the composite element  $\sigma_v\mathcal{T}$ . The first two generators of  $D_{6h}^*$  generate  $C_{6h}$ . Later, we will show the low-energy theory of the chiral flux phase is exactly  $\hat{\Delta}_{\phi,1}$ . The  $\hat{\Delta}_{\phi,2}$  and  $\hat{\Delta}_{\phi,3}$  belongs to  $A_{1g}$  representation of two different  $D_{2h}$  groups which are generated by three generators:  $C_2$  rotation along the  $z$  axis, inversion operator  $\mathcal{I}$ , and  $\sigma'_v$  or  $\sigma''_v$  for different  $D_{2h}$  groups, respectively.

For the diagonal  $\hat{\Delta}_s$  class, the order parameters describe the on-site charge difference.  $\hat{\Delta}_s$  does not involve the scattering between  $M$  points and hence does not need to break the translation symmetry. The order parameters can be classified as

$$\hat{\Delta}_{s,1} = \Delta_{s,1} \left( \frac{\sqrt{3}}{2}\Gamma_3 + \frac{1}{2}\Gamma_8 \right), \quad (12)$$

$$\hat{\Delta}_{s,2} = \Delta_{s,2}\Gamma_8. \quad (13)$$

The  $\hat{\Delta}_{s,1}$ ,  $\hat{\Delta}_{s,2}$  belong to the  $A_{1g}$  representations of two different  $D_{2h}$  groups.

We can also extend the above discussion to more general multiorbital cases. As discussed above, the group of wave vectors at  $M$  point is  $D_{2h}$ .  $D_{2h}$  only contains a one-dimensional (1D) irreducible representations. Hence,  $\psi_{M_i}$  must belong to one of  $D_{2h}$  1D irreducible representations. We can take  $\psi_{M_1}$  as an example. Since  $\psi_{M_1}$  is the eigenstate of  $D_{2h}$  element  $\sigma_v$ , the eigenstate of  $\sigma_v$  can be either  $C_{C\alpha}$  or  $C_{A\alpha} \pm C_{B\beta}$ , where the  $\alpha$  and  $\beta$  are the corresponding orbital index. These  $\alpha$ ,  $\beta$  orbitals should be related to each other by  $\sigma_v$ .  $\psi_{M_{2/3}}$  eigenstates can be found by  $C_3$  rotations.

If the  $\psi_{M_1}$  is still from  $C$  sublattice as  $C_{C\alpha}$ , the  $\psi_{M_2}$  must be also formed by  $C_{A\alpha'}$  and  $\psi_{M_3}$  is formed by  $C_{B\alpha''}$ , where  $\alpha'$  and  $\alpha''$  are orbitals related by  $C_3$  rotation from an  $\alpha$  orbital. Hence, the time-reversal breaking flux phase  $\hat{\Delta}_\phi$  is still corresponding to the complex hopping between each sublattice involving the orbital degree of freedom in the kagome multiorbital systems, like  $C_{C\alpha}^\dagger C_{A\alpha'}$ . On the other hand, if the  $\psi_{M_1}$  is formed by  $C_{A\alpha} \pm C_{B\beta}$ , then  $\psi_{M_2}$  is formed by  $C_{B\alpha'} \pm C_{C\beta'}$  and  $\psi_{M_3}$  is formed by  $C_{A\alpha''} \pm C_{C\beta''}$ . The time-reversal breaking flux phase is still dominated by the complex hopping between each sublattice with a partial part of the on-site orbital polarization density wave, like  $(C_{A\alpha} \pm C_{B\beta})^\dagger (C_{B\alpha'} \pm C_{C\beta'})$ . Besides these cases, any linear combination of  $C_{C\alpha}$  and  $C_{A\alpha} \pm C_{B\beta}$  is also possible as an eigenstate of  $\psi_{M_1}$ , whose flux state is also dominated by the complex hopping.

In short, by using the low-energy model based on the wave functions at three van Hove  $M$  points, we discussed the possible symmetry breaking orders. The time-reversal symmetry breaking state dominated by vH points in the kagome lattice must correspond to the complex hopping flux phase between sublattices for both single and multiorbital models. However, the low-energy model only covers three FS points. The relations between low-energy models and the real space pattern of the charge density waves, charge bonds orders, and chiral flux phases are still undetermined. In the next section we will construct the real space order parameters with the three  $\vec{Q}$  vectors shown in Fig. 1(b), and reveal the relationship between these order parameters and the low-energy models constructed in this section [30].

### III. THE RELATION BETWEEN THE LOW-ENERGY EFFECTIVE MODEL AND THE $3Q$ PATTERN IN REAL SPACE

Besides the low-energy effective model, the chiral flux phase utilizing the real space  $3Q$  configuration and kagome sublattice degree of freedom was proposed to be the reason for time-reversal symmetry breaking in  $AV_3Sb_5$  [24]. The key

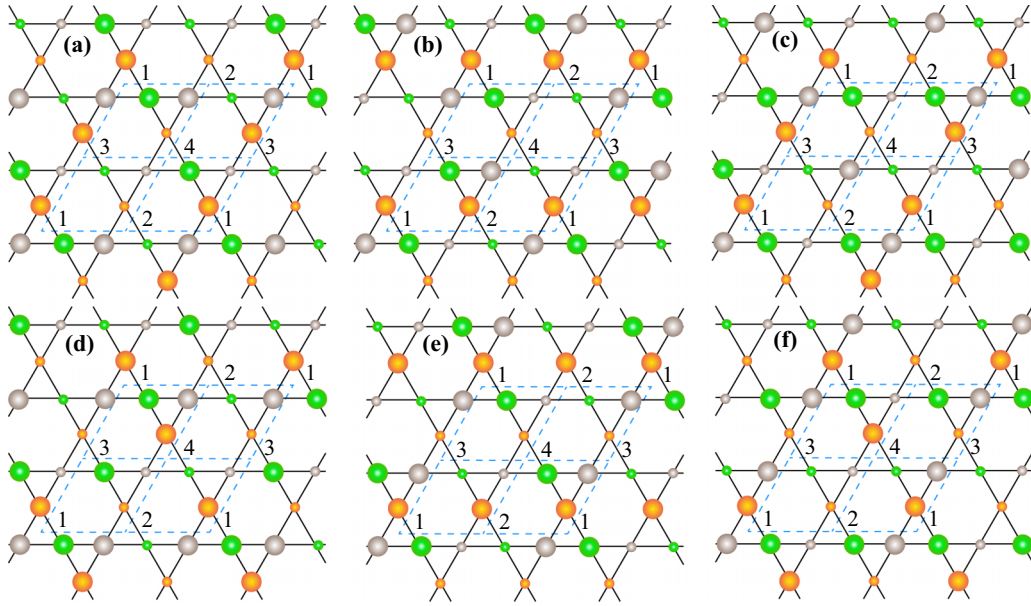


FIG. 2. Six vCDW configurations and their point groups, the size of the dots means the charge density of each site, and different colors mean a different sublattice: (a) vCDW-a ( $C_{3h}$ ), (b) vCDW-b ( $D_{6h}$ ), (c) vCDW-c ( $C_{2v}$ ), (d) vCDW-d ( $C_{2v}$ ), (e) vCDW-e ( $C_{2v}$ ), and (f) vCDW-f ( $C_{3h}$ ).

idea is to find a three component vector and each component forms a density wave  $\cos(\mathbf{Q}_i \cdot \mathbf{r})$  using one of the three scattering momentum  $\mathbf{Q}_i$  between vH points, inspired by previous works in hexagonal lattice vH instabilities [31–39].

The first choice is using the charge density for each sublattice as

$$\hat{\mathbf{n}}(\mathbf{R}_\alpha) = (\hat{n}_{A_\alpha}, \hat{n}_{B_\alpha}, \hat{n}_{C_\alpha}), \quad (14)$$

where the  $\mathbf{R}_\alpha$  is the coordinate for the unit cell formed by the sublattices  $A, B, C$ , here with a  $2 \times 2$  unit cell, it can be divided into four categories:  $2n\mathbf{a}_1 + 2m\mathbf{a}_2 + \{\mathbf{0}, \mathbf{a}_1, \mathbf{a}_2, \mathbf{a}_1 + \mathbf{a}_2\}$  for  $\alpha = 1, 2, 3, 4$ , respectively,  $n, m$  are integers. The  $\mathbf{a}_1$  and  $\mathbf{a}_2$  are defined as before. Hence, the vector charge density wave (vCDW) coupling to this is defined as

$$\Delta_{\text{vCDW}}(\mathbf{R}) = \lambda[\cos(\mathbf{Q}_a \cdot \mathbf{R}), \cos(\mathbf{Q}_b \cdot \mathbf{R}), \cos(\mathbf{Q}_c \cdot \mathbf{R})], \quad (15)$$

where  $\mathbf{Q}_a = \{0, \frac{2\pi}{\sqrt{3}}\}$ ,  $\mathbf{Q}_b = \{-\pi, -\frac{\pi}{\sqrt{3}}\}$ , and  $\mathbf{Q}_c = \{\pi, -\frac{\pi}{\sqrt{3}}\}$ , as shown in Fig. 2(a). Besides this vCDW-a configuration we proposed in the previous work, the other five vCDW configurations (vCDW-b to vCDW-f) can be also found by permutating the wave momentum  $\mathbf{Q}_i$ , as shown in Figs. 2(b)–2(f). Among all the vCDW orders, the vCDW-b state has the highest symmetry with the point-group  $D_{6h}$  and breaking the translation symmetry down to  $2 \times 2$  order. Moreover, vCDW-b is the lowest energy state among all vCDW orders shown in Fig. 2 according to the ground state energy:

$$E_g = \langle g | \hat{H} | g \rangle, \quad (16)$$

where  $\hat{H}$  is the mean-field Hamiltonian of the vCDW state, and  $|g\rangle$  is the corresponding ground state wave function of the mean-field Hamiltonian  $\hat{H}$  at  $5/4$  van Hove filling. For example, the mean-field Hamiltonian of the vCDW-a is

$$\hat{H} = H_0 - \sum_{\mathbf{R}_\alpha} \Delta_{\text{vCDW}}(\mathbf{R}_\alpha) \cdot \hat{\mathbf{n}}(\mathbf{R}_\alpha). \quad (17)$$

It is worth noting that the charge distribution of vCDW-b state has the same configuration as the chiral flux phase in our previous work. Since the chiral flux phase has the magnetic  $D_{6h}(C_{6h})$  group symmetry, the vCDW-b state can coexist with the chiral flux phase and retain its symmetry. In addition, the symmetry of the vCDW-a and vCDW-f are both  $C_{3h}$  and the other remaining three vCDW orders all belong to  $C_{2v}$ , as shown in Figs. 2(c)–2(e).

Another choice is to use the bonds between sublattices:

$$\hat{\mathbf{O}}(\mathbf{R}_\alpha) = (c_{A_\alpha}^\dagger c_{B_\alpha}, c_{B_\alpha}^\dagger c_{C_\alpha}, c_{C_\alpha}^\dagger c_{A_\alpha}). \quad (18)$$

The charge bond order (CBO) with real order parameter is defined as

$$\Delta_{\text{CBO}}(\mathbf{R}) = \lambda[\cos(\mathbf{Q}_a \cdot \mathbf{R}), \cos(\mathbf{Q}_b \cdot \mathbf{R}), \cos(\mathbf{Q}_c \cdot \mathbf{R})] \quad (19)$$

as shown in Fig. 3(a). Similarly, we can also find the other five CBO configurations, as shown in Figs. 3(b)–3(f). The symmetry group of the CBO-a state is  $D_{3h}$ . The CBO-b,c,d orders belong to the  $C_{2v}$  group. And the CBO-e,f belong to the  $C_{3h}$  group. Among all six CBO configurations shown in Fig. 3, the CBO-a has the highest symmetry and the lowest energy, which can be gotten by the same method as in vCDW states.

Interestingly, another two bond orders “anti-tri-hexagonal” (ATH) and “tri-hexagonal” (TrH) in the kagome lattice have been widely discussed [25,27,37,39–41], as shown in Fig. 4. These two bond orders cover all the kagome lattice bonds, which is beyond our above discussion. To include these, the order parameters can be constructed as

$$\begin{aligned} \hat{\mathbf{O}}_1(\mathbf{R}_\alpha) &= (c_{A_\alpha}^\dagger c_{B_\alpha}, c_{B_\alpha}^\dagger c_{C_\alpha}, c_{C_\alpha}^\dagger c_{A_\alpha}), \\ \hat{\mathbf{O}}_2(\mathbf{R}'_\beta) &= (c_{A'_\beta}^\dagger c_{B'_\beta}, c_{B'_\beta}^\dagger c_{C'_\beta}, c_{C'_\beta}^\dagger c_{A'_\beta}), \end{aligned} \quad (20)$$

where  $\mathbf{R}_\alpha$  is the unit cell coordinate defined above and  $\mathbf{R}'_\beta$  is the new coordinate for the unit cell formed by the sublattices

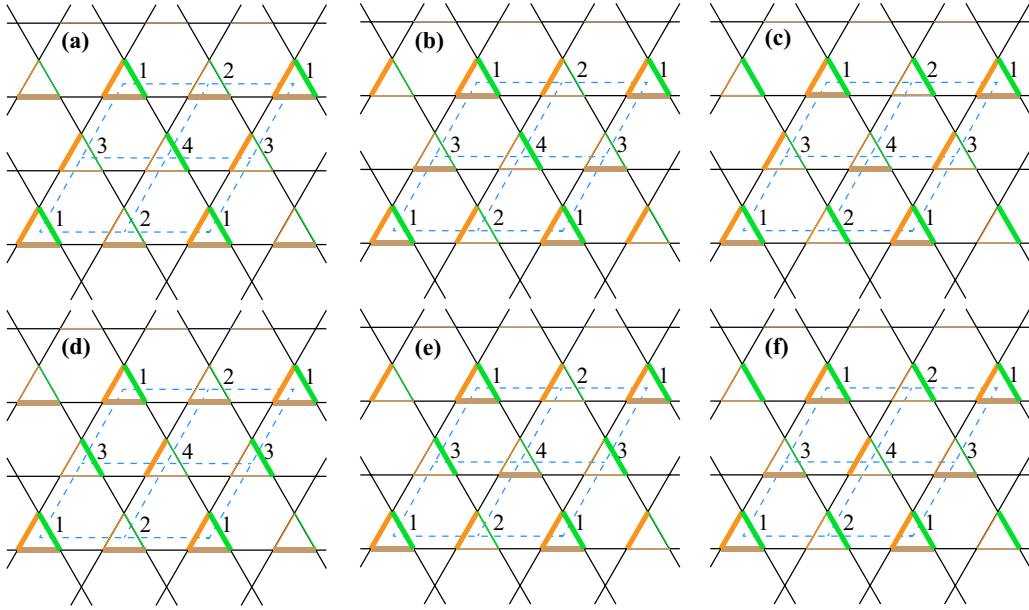


FIG. 3. Six CBO configurations and their point groups, the width of the bond means the relative hopping amplitude, and the color of these bonds mean different hoppings between sublattices: (a) vCBO-a ( $D_{3h}$ ), (b) vCBO-b ( $C_{2v}$ ), (c) vCBO-c ( $C_{2v}$ ), (d) vCBO-d ( $C_{2v}$ ), (e) vCBO-e ( $C_{3h}$ ), and (f) vCBO-f ( $C_{3h}$ ).

$A'$ ,  $B'$ ,  $C'$  shown in Fig. 4(a), and it can be also divided into  $2n\mathbf{a}_1 + 2m\mathbf{a}_2 + \{\mathbf{0}, \mathbf{a}_1, \mathbf{a}_2, \mathbf{a}_1 + \mathbf{a}_2\}$  for  $\beta = 1', 2', 3', 4'$ , respectively,  $n, m$  are integers. The Hamiltonian can be expressed as

$$H_{\text{CBO}} = H_0 - \sum_{\mathbf{R}_\alpha} \Delta_{\text{CBO}}(\mathbf{R}_\alpha) \cdot \hat{\mathbf{O}}_1(\mathbf{R}_\alpha) - \sum_{\mathbf{R}'_\beta} \Delta_{\text{CBO}}(\mathbf{R}'_\beta) \cdot \hat{\mathbf{O}}_2(\mathbf{R}'_\beta), \quad (21)$$

where  $\Delta_{\text{CBO}}(\mathbf{R}'_\beta)$  is using the same density-wave vectors as in Eq. (17). Hence, the ATH and TrH also utilize the three  $Q$  scattering mechanisms discussed above. The symmetry group of ATH and TrH is  $D_{6h}$ . And the low-energy effective model of ATH and TrH correspond to  $\hat{\Delta}_{b,1}$ , which form the  $A_{1g}$  representation of  $D_{6h}$  (see the Supplemental Material (SM) for details [30]). In addition to ATH and TrH, the ‘‘Star of

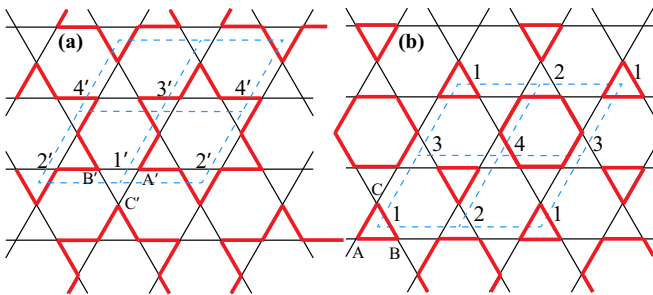


FIG. 4. (a) Anti-tri-hexagonal bond order configuration. In order to cover all bonds, we also define another coordinate for the kagome lattice, labeled as  $A'$ ,  $B'$ ,  $C'$ . To utilize the three  $Q$  pattern, the unit cell name of the new coordinate is also shifted to  $1'$ ,  $2'$ ,  $3'$ ,  $4'$ . The red bonds mean the hopping in these bonds are a strengthened (b) tri-hexagonal bond order configuration.

David’’ (SoD) state is another widely proposed configuration [20,40,42], as shown in Fig. 10(c). Notice that the SoD state looks quite similar to the ATH bond order, which also belongs to  $D_{6h}$  point group and  $\hat{\Delta}_{b,1}$  effective theory. The TrH state is always the lowest energy state among all the charge bond order states in our calculation. In the next section we will also discuss the possible CBOs with  $C_6$  symmetry.

Finally, if the order parameters coupled to bonds are imaginary, the chiral flux phase can be found:

$$\Delta_{\text{CFP}}(\mathbf{R}) = i\lambda[\cos(\mathbf{Q}_a \cdot \mathbf{R}), \cos(\mathbf{Q}_b \cdot \mathbf{R}), \cos(\mathbf{Q}_c \cdot \mathbf{R})]. \quad (22)$$

Further adding other terms, the Hamiltonian for CFP can be expressed as

$$H_{\text{CFP}} = H_0 - \sum_{\mathbf{R}_\alpha} \Delta_{\text{CFP}}(\mathbf{R}_\alpha) \cdot \hat{\mathbf{O}}_1(\mathbf{R}_\alpha) - \sum_{\mathbf{R}'_\beta} \Delta_{\text{CFP}}(\mathbf{R}'_\beta) \cdot \hat{\mathbf{O}}_2(\mathbf{R}'_\beta). \quad (23)$$

The low-energy effective theory of CFP corresponds to  $\hat{\Delta}_{\phi,1}$ , which belongs to  $A_{1g}$  representation of  $D_{6h}^*(C_{6h})$  magnetic group as discussed in Sec. II. Besides this CFP state, we find 122 flux phases in the kagome lattice with a  $2*2$  configuration, which will be discussed in the next section.

#### IV. ALL POSSIBLE FLUX PHASES IN THE KAGOME LATTICE WITHIN A $2*2$ UNIT CELL

The above discussion focuses on the low-energy scattering between vH points, which leads to the promising states, chiral flux phase. Are there other flux phases in the kagome lattice? To answer this question, we should find a general principle. Generally speaking, a current operator from site  $j$  to site  $i$  can

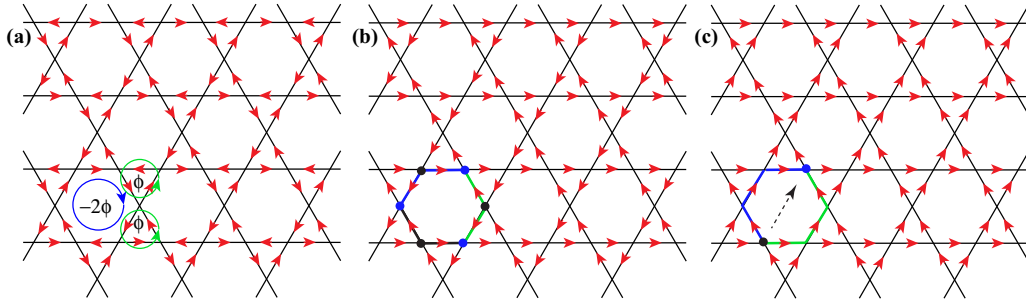


FIG. 5.  $1*1$  flux configurations. (a) Nagaosa solution with  $-2\phi$  flux at each hexagon and  $\phi$  flux at each triangle. (b) Flow-b solution with three charge sinks (blue dot) and three charge sources (black dot) at each hexagon. (c) Flow-b solution with a one charge sink (blue dot) and a one charge source (black dot) at each hexagon. The dashed black arrow indicates the flow direction at each hexagon.

be found to be

$$\hat{\mathbf{J}}_{ij} = \frac{e}{i\hbar} \{t_{ij}C_i^\dagger C_j - t_{ij}^*C_j^\dagger C_i\}, \quad (24)$$

where  $t_{ij}$  is the hopping parameter from site  $j$  to site  $i$ . Therefore, the expectation value of the current operator can only be finite when  $t_{ij}$  contains an imaginary part, which corresponds to the flux state. For any current state, the charge continuity equation  $\frac{\partial \rho}{\partial t} + \nabla \cdot \mathbf{J} = 0$  must be satisfied, where  $\rho$  is the charge density. Therefore, to find all possible flux solutions, there is only one principle: the currents must conserve at each lattice site without generating any charge sink or source. To simplify our discussion, we also assume that the amplitudes of the complex hopping terms at all bonds must be the same. Generally speaking, the physical system always favors the high symmetry state. The equal number of arrows going in and out is enough for general cases, such as the Haldane model [1], the loop-current model [5], and the  $d$ -density wave model [6].

Following the above constraints, we find 183 flux phases in the kagome lattice within the  $2*2$  unit cell. Specifically, there are 10 flux phases in the  $1*1$  unit cell, 122 phases in the  $2*2$  unit cell, and the remaining  $17*3$  in the  $1*2$  unit cell, which is discussed separately in the following subsections.

### A. $1*1$ configuration

The first flux phase in the kagome lattice is initially proposed by Ohgushi, Murakami, and Nagaosa [43], which mapped a spin itinerant system with nonzero spin chirality to a flux phase in the kagome lattice. We name this phase as the Nagaosa solution, as shown in Fig. 5(a). At each kagome triangle there is one flux  $\phi$  owing to the complex hopping along the triangle loop. Another flux with  $-2\phi$  penetrates each kagome hexagonal plaquette. The quantum anomalous Hall effect is also obtained in this Nagaosa solution [43]. By

TABLE II. Three classes of flux phase in a  $1*1$  unit cell. The number of configurations at each class is also listed in parentheses.

| Symmetry              | Class name  |
|-----------------------|-------------|
| $D_{6h}^*(C_{6h})$    | Nagaosa (2) |
| $D_{6h}^{*2}(D_{3h})$ | Flow-a (2)  |
| $D_{2h}^*(C_{2v})$    | Flow-b (6)  |

reversing the current direction, a second Nagaosa solution can also be obtained.

We can also understand the Nagaosa solution from another point of view. As shown in Fig. 5, the kagome lattice contains three kinds of bond directions. For the Nagaosa solution, the current direction alternates in each bond direction. Therefore, if the currents all flow in the same direction, the other  $1*1$  flux configurations can be found. Among these  $2^3$  configurations, we also find two classes named flow-a solution and flow-b solution, respectively. For flow-a solution, there are three charge sinks and three charge sources at each hexagon, as shown in Fig. 5(b). Owing to charge conservation, the sinks become sources at the neighboring hexagon. Flow-a class contains two configurations. On the other hand, there is one sink and one source at each hexagonal plaquette diagonal direction for flow-b solution, as shown in Fig. 5(c). The net flow direction at each hexagon is also labeled as a dashed black arrow. Since there are also three diagonal directions, the flow-b class contains  $2*3$  configurations.

In all of these three classes, Nagaosa solution and flow-a solution only break time-reversal symmetry and preserve all the point-group symmetry of the kagome lattice. Their symmetry can be described by magnetic group  $D_{6h}^*$ . Since the invariant subgroup of  $D_{6h}$  can be either  $C_{6h}$  or  $D_{3h}$ , there are two kinds of magnetic groups. The symmetry of Nagaosa solution can be described by group  $D_{6h}^*(C_{6h})$ , while the symmetry of flow-a solution can be described by

TABLE III. 18 classes of flux phase in a  $2*2$  unit cell and their symmetry groups. The number of configurations at each class is also listed in parentheses.

| Symmetry              | Class name  |
|-----------------------|---|
| $D_{6h}^*(C_{6h})$    | $D_{6a}$ (2), $D_{6b}$ (2), $D_{6c}$ (2)  |
| $D_{6h}^{*2}(D_{3h})$ | $D'_{6a}$ (2)   |
| $D_{3h}^*(C_{3h})$    | $D_{3a}$ (4), $D_{3b}$ (4), $D_{3c}$ (4)  |
| $D_{2h}^*(C_{2h})$    | $D_{2a}$ (6)  |
| $C_{2v}^*$            | $C_{2a}$ (6), $C_{2b}$ (12), $C_{2c}$ (12), $C_{2d}$ (12), $C_{2e}$ (12), $C_{2f}$ (12), $C_{2g}$ (6), $C_{2h}$ (6) |
| $C_{2v}'$             | $C'_2$ (6)  |
| $C_2$                 | $C''_2$ (12)  |

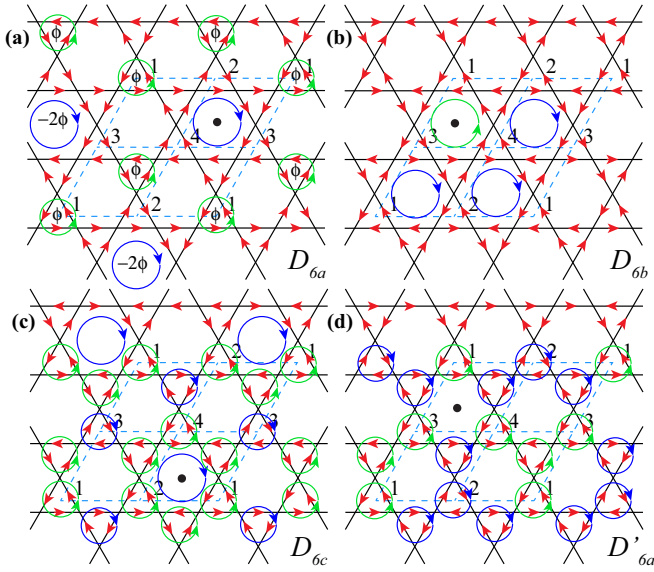


FIG. 6.  $2*2$  flux configurations. (a)  $D_{6a}$  class with  $-2\phi$  flux forming a triangle lattice and  $\phi$  flux forming a honeycomb lattice. (b)  $D_{6b}$  class with one positive flux hexagon and three negative flux hexagons. (c)  $D_{6c}$  class with flipping the two diagonal triangle fluxes of three hexagons. (d)  $D'_{6a}$  class with three opposite flux triangle loops at each hexagon. The inversion center of each class is also highlighted by black dots.

$D_{6h}^{*2}(D_{3h})$ . Additionally, the flow-b solution breaks both time-reversal symmetry and point-group symmetry, which belongs to  $D_{2h}^{*}(C_{2v})$  magnetic group (Table II).

### B. $2*2$ configuration

The symmetry breaking orders with a  $2*2$  unit cell are the most important configurations we focus on. We search

all possible configurations by the brute-force approach and project out the configurations violating the charge conservation rule. We find 122 flux phases with a  $2*2$  unit cell. Among the 122 configurations, there are 18 classes, as summarized in Table III and shown in Figs. 6–8.  $D_{6a}$  state is found to be the lowest energy state among all these flux states.

Similar to the previous discussion, there are four classes that only break the time-reversal symmetry. Since the invariant subgroup of  $D_{6h}$  can be either  $C_{6h}$  or  $D_{3h}$ , these four classes can belong to different magnetic group  $D_{6h}^{*}(C_{6h})$  or  $D_{6h}^{*2}(D_{3h})$ , as listed in Table III. For the  $D_{6h}^{*}(C_{6h})$  group, we find three classes  $D_{6a}$ ,  $D_{6b}$ , and  $D_{6c}$ , as shown in Figs. 6(a)–6(c). The  $D_{6a}$  is the CFP state we proposed in the previous work [24], where two  $\phi$  fluxes form a honeycomb lattice with another  $-2\phi$  form a triangle lattice.  $D_{6a}$  class only contains two configurations related to time reversal.

$D_{6b}$  class can be viewed as flipping one hexagon flux of the four four hexagon plaquettes by enlarging the Nagaosa configuration to a  $2*2$  unit cell, as shown in Fig. 6(b). The remaining  $D_{6c}$  class is found by flipping the two diagonal triangle fluxes of the three hexagons in a  $2*2$  unit cell, as shown in Fig. 6(c). The low-energy effective model for  $D_{6b}$  and  $D_{6c}$  also correspond to  $\Gamma_2 - \Gamma_5 + \Gamma_7$  (see the SM Sec. 1 for details [30]). For  $D_{6h}^{*2}(D_{3h})$  group, we flip three triangle fluxes of each hexagon plaquette, as shown in Fig. 6(d). Both  $D_{6b,c}$  and  $D'_{6a}$  only contains two configurations related by time reversal.

Besides the above classes, other classes break both time-reversal symmetry and point-group symmetry. We find  $D_{3h}^{*}(C_{3h})$ ,  $D_{2h}^{*}(C_{2h})$ ,  $C_{2v}^{*}$ ,  $C_{2v}$ , and  $C_2$  groups. There are three classes belonging to  $D_{3h}^{*}(C_{3h})$  as shown in Figs. 7(a)–7(c). The category with eight classes is  $C_{2v}^{*}$ , as shown in Figs. 8(a)–8(h). As for  $D_{2h}^{*}(C_{2h})$ ,  $C_{2v}$ ,  $C_2$ , there is only one class in each category, as shown in Figs. 7(d), 7(e), and 7(f), respectively. The numbers of configurations for each class are summarized in Table III.

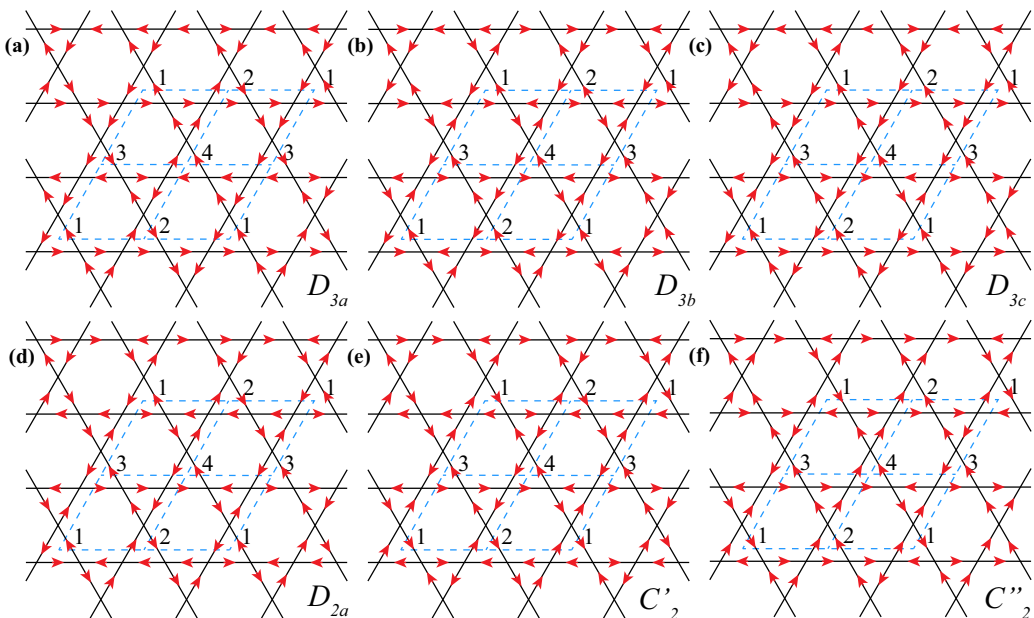


FIG. 7.  $2*2$  flux configuration: (a)  $D_{3a}$  class, (b)  $D_{3b}$  class, (c)  $D_{3c}$  class, (d)  $D_{2a}$  class, (e)  $C'_2$  class, and (f)  $C''_2$  class.

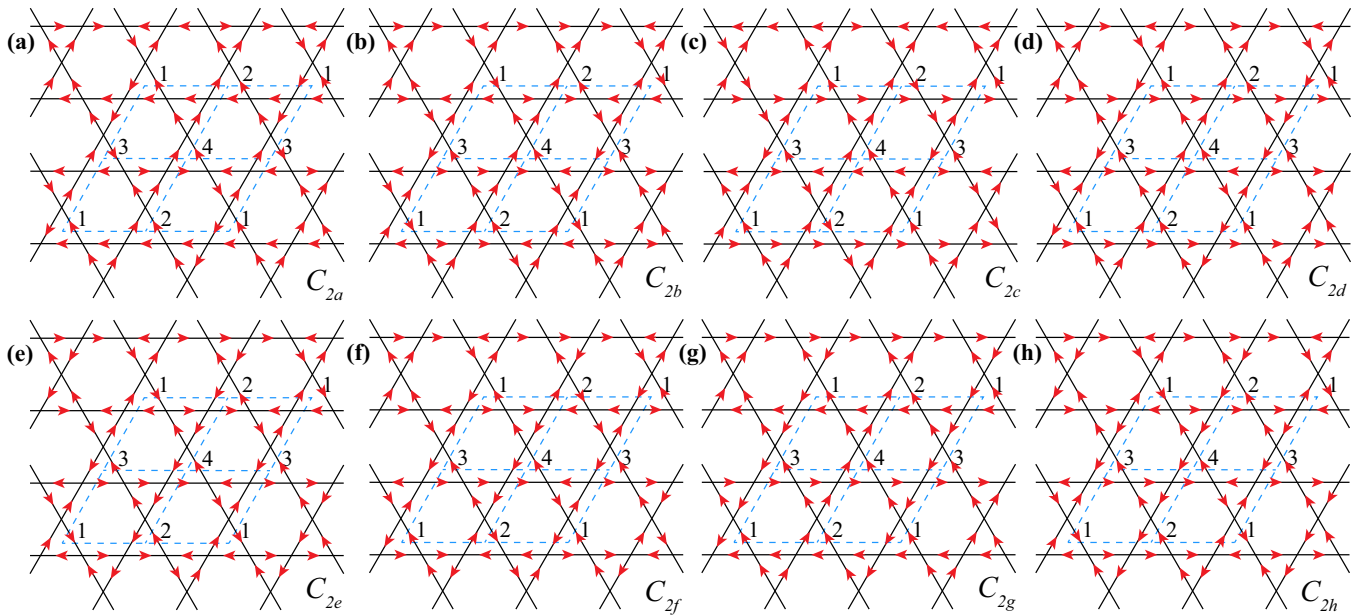


FIG. 8.  $2*2$  flux configurations: (a)  $C_{2a}$  class, (b)  $C_{2b}$  class, (c)  $C_{2c}$  class, (d)  $C_{2d}$  class, (e)  $C_{2e}$  class, (f)  $C_{2f}$  class, (g)  $C_{2g}$  class, and (h)  $C_{2h}$  class.

Note that the above flux constructing method is based on real space without considering the low-energy  $3Q$  scattering at  $5/4$  filling. Therefore, most of them are not relevant to  $AV_3Sb_5$ . For example, the  $C_{2g}$ ,  $C_{2h}$ ,  $C_{2'}$ , and  $C_{2''}$  configurations are gapless at  $\nu_H$  filling.

### C. $1*2$ configuration

To complete our discussion on flux phases, we also list all the  $1*2$  configurations. There are 17 flux phases in a  $1$  by  $2$  unit cell, which only contain eight classes (Table IV), as

shown in Fig. 9. Since there are three translation directions in the kagome lattice, there are also other  $2*17$  flux phases by breaking translation symmetry in the other two directions.

These eight classes can be divided into three categories by symmetry, all of them break both time-reversal symmetry and point-group symmetry. Similar to magnetic group  $D_{6h}^*$ , the invariant subgroup of the magnetic group  $D_{2h}^*$  can be either  $C_{2h}$  or  $C_{2v}$ . Thus, there are two kinds of magnetic groups. The classes shown in Figs. 9(a) and 9(b) belong to  $D_{2h}^{*1}(C_{2h})$ , while the class shown in Fig. 9(c) belongs to  $D_{2h}^{*2}(C_{2v})$ . The other five classes belong to  $C_{2v}^*(C_2)$  as shown in Figs. 9(d)–9(h).

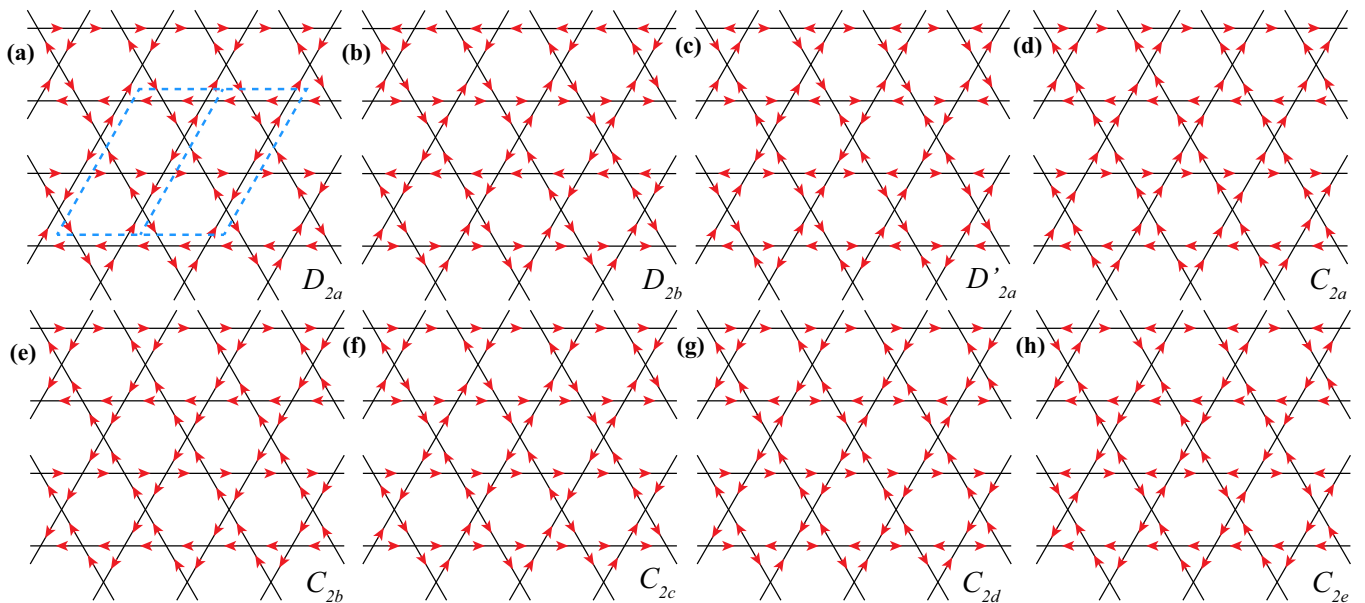


FIG. 9.  $1*2$  flux configurations: (a)  $D_{2a}$  class, (b)  $D_{2b}$  class, (c)  $D'_{2a}$  class, (d)  $C_{2a}$  class, (e)  $C_{2b}$  class, (f)  $C_{2c}$  class, (g)  $C_{2d}$  class, and (h)  $C_{2e}$  class.



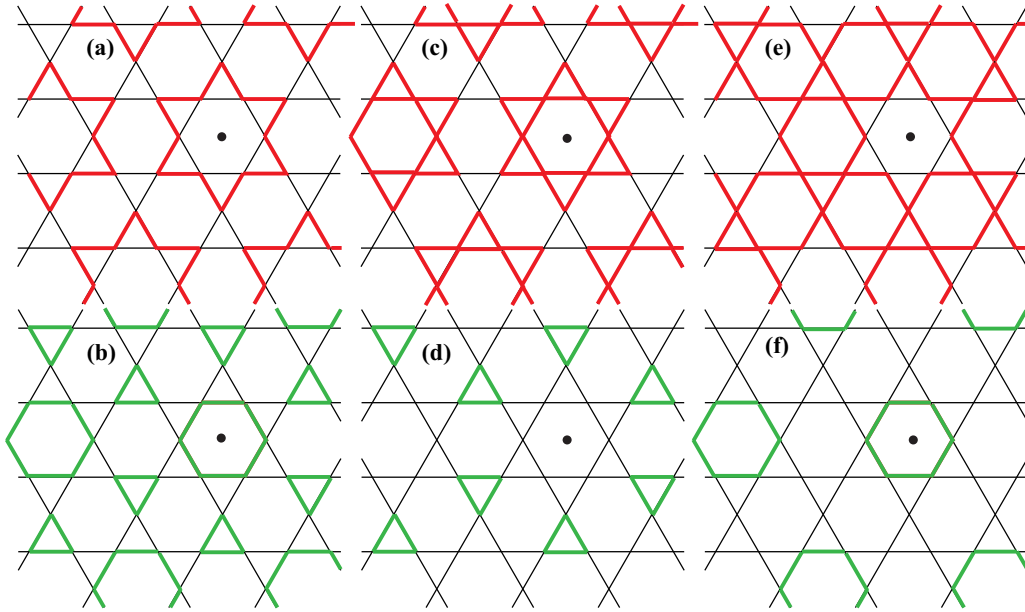


FIG. 10. CBO configurations with  $D_{6h}$  symmetry: (a)  $D_{6a}$  or ATH, (b)  $ID_{6a}$  or TrH, (c)  $D_{6b}$  or SoD, (d)  $ID_{6b}$  or ISoD, and (e)  $D_{6c}$ . (f)  $ID_{6c}$ .

#### D. $C_6$ symmetric CDW and CBO

Besides the above flux states, finding other charge density wave and charge bond order states is also an interesting task. Compared to flux states, CDW could have a  $2^{12}$  possible configurations and CBO could have a  $2^{24}$  possible configurations within a  $2 \times 2$  unit cell, which seems to be an impossible work. However, we can use symmetry constraint to focus on high symmetry configurations. Utilizing the  $C_6$  rotation symmetry constraint, we search all possible  $C_6$  symmetric CDWs and CBOs. For CDW state we only find two states with a positive or negative charge vCDW-b configuration. For CBO states we find six CBOs with  $D_{6h}$  point-group symmetry and four CBOs with  $C_{6h}$  point-group symmetry, as shown in Figs. 10 and 11.

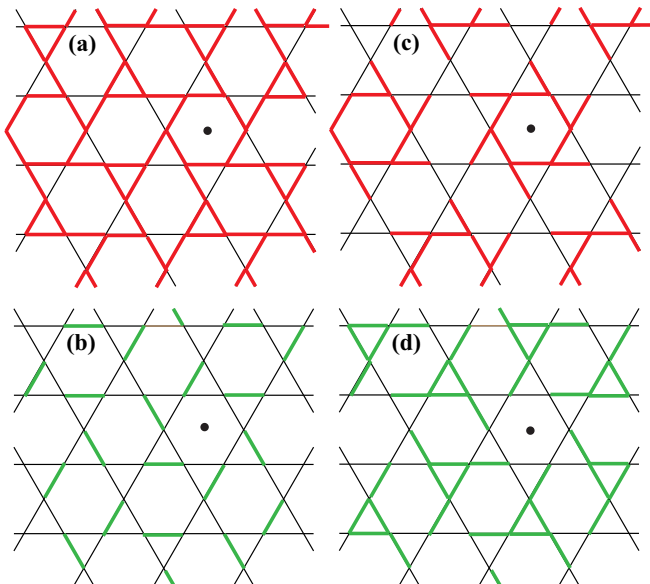


FIG. 11. CBO configurations with  $C_{6h}$  symmetry: (a)  $C_{6a}$ , (b)  $IC_{6a}$ , (c)  $C_{6b}$ , and (d)  $IC_{6b}$ .

In Fig. 10 the up panel states are labeled as  $D_{6a}$ ,  $D_{6b}$ , and  $D_{6c}$  while the down panel states are inverse configurations of the up panel labeled as  $ID_{6a}$ ,  $ID_{6b}$ , and  $ID_{6c}$ . The  $D_{6a}$  state is ATH, the  $ID_{6a}$  is TrH, and the  $D_{6b}$  is SoD as defined above. Notice that  $ID_{6b}$  is the ‘‘inverse Star of David’’ (ISoD) rather than  $ID_{6a}$ . Similarly, we also label the  $C_{6h}$  symmetry configurations as  $C_{6a}$ ,  $C_{6b}$  and  $IC_{6a}$ ,  $IC_{6b}$ , as shown in Fig. 11.

#### V. DISCUSSION AND SUMMARY

In summary, the time-reversal symmetry breaking CDW found in  $AV_3Sb_5$  provides a new platform to investigate correlation and topology. By analyzing the dominated van Hove points around the Fermi surface and corresponding symmetry properties, the low-energy effective theory for the kagome lattice at vH filling can be constructed. All symmetry breaking states of this vH low-energy effective theory can be found and classified according to the point group. The relations between low-energy symmetry breaking states to the physical orders in real space can be fully established. The above study based on a single orbital model on the kagome lattice can be straightforwardly generalized to multiorbital cases. The dominated time-reversal breaking channel is always the flux phase. The full flux configurations that satisfy the charge conservation rule include 183 flux phases in the kagome lattice within a  $2 \times 2$  unit cell. Especially, we list all 3, 18, and 8 classes which

TABLE IV. Eight classes of flux phase in the  $1 \times 2$  unit cell. The number of configurations at each class is also listed in parentheses.

| Symmetry              | Class name  |
|-----------------------|---|
| $D_{2h}^{*1}(C_{2h})$ | $D_{2a}(1), D_{2b}(1)$ ,                                |
| $D_{2h}^{*2}(C_{2v})$ | $D'_{2a}(1)$  |
| $C_{2v}^*(C_2)$       | $C_{2a}(2), C_{2b}(2), C_{2c}(2), C_{2d}(4), C_{2e}(4)$ |

are independent in symmetry belonging to  $1*1$ ,  $2*2$ , and  $1*2$  unit cells in Tables II, III, and IV, respectively. The symmetry classifications and relations to low-energy effective theory of these flux phases are obtained. All these findings give rise to complete analysis and new understandings of flux phases in the kagome lattice.

Note that, when finalizing this work, several theoretical works starting from low-energy effective theory appeared [26,27]. Reference [26] analyzed the real and imaginary CDW at vH singularity on the hexagonal lattices from a phenomenological Ginzburg-Landau theory. Reference [27] studied the electronic instabilities of the kagome lattice using

a parquet renormalization group and corresponding Landau theory.

## ACKNOWLEDGMENTS

We thank Xi Dai, Li Yu, Hu Miao, and Ziqiang Wang for useful discussions. This work is supported by the Ministry of Science and Technology (Grant No. 2017YFA0303100), National Science Foundation of China (Grant No. NSFC-11888101), and the Strategic Priority Research Program of Chinese Academy of Sciences (Grant No. XDB28000000). K.J. acknowledges support from the start-up grant of IOP-CAS.

- 
- [1] F. D. M. Haldane, *Phys. Rev. Lett.* **61**, 2015 (1988).  
 [2] I. Affleck and J. B. Marston, *Phys. Rev. B* **37**, 3774(R) (1988).  
 [3] M. U. Ubbens and P. A. Lee, *Phys. Rev. B* **46**, 8434 (1992).  
 [4] P. A. Lee, N. Nagaosa, and X.-G. Wen, *Rev. Mod. Phys.* **78**, 17 (2006).  
 [5] C. M. Varma, *Phys. Rev. B* **55**, 14554 (1997).  
 [6] S. Chakravarty, R. B. Laughlin, D. K. Morr, and C. Nayak, *Phys. Rev. B* **63**, 094503 (2001).  
 [7] C. M. Varma, *Phys. Rev. B* **73**, 155113 (2006).  
 [8] M. R. Norman, D. Pines, and C. Kallin, *Adv. Phys.* **54**, 715 (2005).  
 [9] B. Keimer, S. A. Kivelson, M. R. Norman, S. Uchida, and J. Zaanen, *Nature (London)* **518**, 179 (2015).  
 [10] J. W. F. Venderbos, *Phys. Rev. B* **93**, 115107 (2016).  
 [11] Y. X. Zhang, H. M. Guo, and R. T. Scalettar, *Phys. Rev. B* **101**, 205139 (2020).  
 [12] C. Nayak, *Phys. Rev. B* **62**, 4880 (2000).  
 [13] C.-C. Chang and R. T. Scalettar, *Phys. Rev. Lett.* **109**, 026404 (2012).  
 [14] S. Hayami, Y. Yanagi, H. Kusunose, and Y. Motome, *Phys. Rev. Lett.* **122**, 147602 (2019).  
 [15] J. Liu, S. Y. Park, K. F. Garrity, and D. Vanderbilt, *Phys. Rev. Lett.* **117**, 257201 (2016).  
 [16] Z.-X. Luo, C. Xu, and C.-M. Jian, *Phys. Rev. B* **104**, 035136 (2021).  
 [17] N. E. Shaik, B. Dalla Piazza, D. A. Ivanov, and H. M. Rønnow, *Phys. Rev. B* **102**, 214413 (2020).  
 [18] B. R. Ortiz, L. C. Gomes, J. R. Morey, M. Winiarski, M. Bordelon, J. S. Mangum, I. W. H. Oswald, J. A. Rodriguez-Rivera, J. R. Neilson, S. D. Wilson, E. Ertekin, T. M. McQueen, and E. S. Toberer, *Phys. Rev. Mater.* **3**, 094407 (2019).  
 [19] B. R. Ortiz, S. M. L. Teicher, Y. Hu, J. L. Zuo, P. M. Sarte, E. C. Schueller, A. M. Milinda Abeykoon, M. J. Krogstad, S. Rosenkranz, R. Osborn, R. Seshadri, L. Balents, J. He, and S. D. Wilson, *Phys. Rev. Lett.* **125**, 247002 (2020).  
 [20] Y.-X. Jiang, J.-X. Yin, M. M. Denner, N. Shumiya, B. R. Ortiz, G. Xu, Z. Guguchia, J. He, M. S. Hossain, X. Liu, J. Ruff, L. Kautzsch, S. S. Zhang, G. Chang, I. Belopolski, Q. Zhang, T. A. Cochran, D. Multer, M. Litskevich, Z.-J. Cheng, X. P. Yang, Z. Wang, R. Thomale, T. Neupert, S. D. Wilson, and M. Z. Hasan, *Nat. Mater.* **20**, 1353 (2021).  
 [21] S.-Y. Yang, Y. Wang, B. R. Ortiz, D. Liu, J. Gayles, E. Derunova, R. Gonzalez-Hernandez, L. Āmejkal, Y. Chen, S. S. P. Parkin, S. D. Wilson, E. S. Toberer, T. McQueen, and M. N. Ali, *Sci. Adv.* **6**, eabb6003 (2020).  
 [22] F. H. Yu, T. Wu, Z. Y. Wang, B. Lei, W. Z. Zhuo, J. J. Ying, and X. H. Chen, *Phys. Rev. B* **104**, L041103 (2021).  
 [23] L. Yu, C. Wang, Y. Zhang, M. Sander, S. Ni, Z. Lu, S. Ma, Z. Wang, Z. Zhao, H. Chen, K. Jiang, Y. Zhang, H. Yang, F. Zhou, X. Dong, S. L. Johnson, M. J. Graf, J. Hu, H.-J. Gao, and Z. Zhao, *arXiv:2107.10714*.  
 [24] X. Feng, K. Jiang, Z. Wang, and J. Hu, *Sci. Bull.* **66**, 1384 (2021).  
 [25] M. M. Denner, R. Thomale, and T. Neupert, *arxiv:2103.14045*.  
 [26] Y.-P. Lin and R. M. Nandkishore, *Phys. Rev. B* **104**, 045122 (2021).  
 [27] T. Park, M. Ye, and L. Balents, *Phys. Rev. B* **104**, 035142 (2021).  
 [28] Y. Gu, Y. Zhang, X. Feng, K. Jiang, and J. Hu, *arXiv:2108.04703*.  
 [29] K. Jiang, T. Wu, J.-X. Yin, Z. Wang, M. Zahid Hasan, S. D. Wilson, X. Chen, and J. Hu, *arXiv:2109.10809*.  
 [30] See Supplemental Material at <http://link.aps.org/supplemental/10.1103/PhysRevB.104.165136> for Sec. 1: Basis transformation and relations between  $3Q$  scattering and  $3Q$  pattern in real space. Section 2: Gauge transformation and translation operations.  
 [31] I. Martin and C. D. Batista, *Phys. Rev. Lett.* **101**, 156402 (2008).  
 [32] T. Li, *Europhys. Lett.* **97**, 37001 (2012).  
 [33] S. Hayami and Y. Motome, *Phys. Rev. B* **90**, 060402(R) (2014).  
 [34] S.-L. Yu and J.-X. Li, *Phys. Rev. B* **85**, 144402 (2012).  
 [35] R. Nandkishore, L. Levitov, and A. Chubukov, *Nat. Phys.* **8**, 158 (2012).  
 [36] W.-S. Wang, Y.-Y. Xiang, Q.-H. Wang, F. Wang, F. Yang, and D.-H. Lee, *Phys. Rev. B* **85**, 035414 (2012).  
 [37] M. L. Kiesel, C. Platt, W. Hanke, D. A. Abanin, and R. Thomale, *Phys. Rev. B* **86**, 020507(R) (2012).  
 [38] W.-S. Wang, Z.-Z. Li, Y.-Y. Xiang, and Q.-H. Wang, *Phys. Rev. B* **87**, 115135 (2013).  
 [39] M. L. Kiesel, C. Platt, and R. Thomale, *Phys. Rev. Lett.* **110**, 126405 (2013).  
 [40] B. R. Ortiz, S. M. L. Teicher, L. Kautzsch, P. M. Sarte, J. P. C. Ruff, R. Seshadri, and S. D. Wilson, *arXiv:2104.07230*.  
 [41] E. Uykur, B. Ortiz, S. Wilson, M. Dressel, and A. Tsirlin, *arXiv:2103.07912*.  
 [42] H. Tan, Y. Liu, Z. Wang, and B. Yan, *Phys. Rev. Lett.* **127**, 046401 (2021).  
 [43] K. Ohgushi, S. Murakami, and N. Nagaosa, *Phys. Rev. B* **62**, 6065(R) (2000).